

# Crystallographic Correlations with Anisotropic Oxide Ion Conduction in Aluminum-Doped Neodymium Silicate Apatite Electrolytes

An, Tao; Baikie, Tom; Wei, Fengxia; Pramana, Stevin S.; Schreyer, Martin K.; Piltz, Ross O.;  
Shin, J. Felix; Wei, Jun; Slater, Peter R.; White, Timothy John

2013

An, T., Baikie, T., Wei, F., Pramana, S. S., Schreyer, M. K., Piltz, R. O., et al. (2013).  
Crystallographic Correlations with Anisotropic Oxide Ion Conduction in Aluminum-Doped  
Neodymium Silicate Apatite Electrolytes. *Chemistry of Materials*, 25(7), 1109-1120.

<https://hdl.handle.net/10356/85584>

<https://doi.org/10.1021/cm4000685>

---

© 2013 American Chemical Society. This is the author created version of a work that has  
been peer reviewed and accepted for publication by *Chemistry of Materials*, American  
Chemical Society. It incorporates referee's comments but changes resulting from the  
publishing process, such as copyediting, structural formatting, may not be reflected in this  
document. The published version is available at: [<http://dx.doi.org/10.1021/cm4000685>].

*Downloaded on 13 Mar 2024 17:57:26 SGT*

# Crystallographic Correlations with Anisotropic Oxide Ion Conduction in Aluminum-doped Neodymium Silicate Apatite Electrolytes

Tao An,<sup>†</sup> Tom Baikie,<sup>†</sup> Fengxia Wei,<sup>†</sup> Stevin S. Pramana,<sup>†</sup> Martin K. Schreyer,<sup>‡</sup> Ross O. Piltz,<sup>§</sup> J. Felix Shin,<sup>⊥</sup> Christian Kloc,<sup>†</sup> Jun Wei,<sup>#</sup> Peter R. Slater,<sup>⊥</sup> and Tim J. White<sup>\*,†</sup>

<sup>†</sup>Nanyang Technological University, School of Materials Science and Engineering, 50 Nanyang Avenue, 639798, Singapore, <sup>‡</sup>Institute of Chemical Engineering Sciences (ICES), Agency for Science, Technology and Research (A\*STAR), 1 Pesek Road, Jurong Island, 627833, Singapore, <sup>§</sup>Bragg Institute, Australian Science and Technology Organisation, Lucas Heights, NSW 2234, Australia, <sup>⊥</sup>School of Chemistry, University of Birmingham, Edgbaston, Birmingham, B15 2TT, UK, and <sup>#</sup>Singapore Institute of Manufacturing Technology (SIMTech), Agency for Science, Technology and Research (A\*STAR), 71 Nanyang Drive, 638075, Singapore.

**KEYWORDS** : solid electrolyte, apatite, neodymium silicate, Al-doping, crystal structure, oxide ion conduction

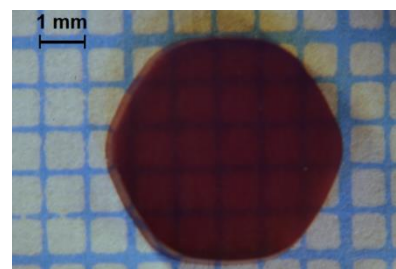
**ABSTRACT**: To better understand the oxide ion conduction mechanism of rare earth silicate apatites as intermediate temperature electrolytes for solid oxide fuel cells (SOFC), the effect of lower valent metal doping on the performance of dense polycrystalline  $\text{Nd}_{(28+x)/3}\text{Al}_x\text{Si}_{6-x}\text{O}_{26}$  ( $0 \leq x \leq 2$ ) ceramics, fabricated using spark plasma sintering (SPS), was compared with large single crystals. Powder X-ray diffraction confirmed that the ceramics were composed principally of apatite, with minor ( $< 10$  wt%) secondary phases ( $\text{Nd}_2\text{SiO}_5$ ,  $\text{NdAlO}_3$  and  $\text{Nd}_2\text{O}_3$ ) in the  $x = 0.5$  and  $x = 2.0$  samples. Scanning electron microscopy of the SPS materials revealed crystals from  $1 - 10 \mu\text{m}$  and grain boundaries devoid of a significant glassy phase. The measurement of ionic conductivity via AC impedance spectroscopy showed that for  $0.5 \leq x \leq 1.5$  the conductivity was enhanced by Al-doping, while for  $x = 2.0$  it was lowered due to the elimination of cation vacancies and the absence of interstitial oxygen. The conductivities of single crystals ( $0 \leq x \leq 1.5$ ) were anisotropic and superior to the sintered pellets. It was deduced that in the best performing polycrystalline samples an increase in  $ab$  basal plane conductivity offset the decline in  $c$ -axis conductivity, due to the progressive decrease in  $\text{Nd}^{3+}$  cation vacancies accompanying the incorporation of  $\text{Al}^{3+}$  with the probable conversion of  $\text{Si}_2\text{O}_7$  entities to  $\text{SiO}_4/\text{SiO}_5$  units that favor  $\text{O}^{2-}$  percolation. Single crystal X-ray diffraction found the undoped crystal conformed to  $P6_3/m$ , but with the O(3) oxygen positions, that participate in conduction, split non-statistically across two sites with a shortened Si-O(3) bond. Consequently, the bond valence sum (BVS) of the Si (4.20) is larger than the formal valence. Fourier difference maps of the Al-doped crystals contain regions of excess scattering, suggesting the possible lowering of symmetry or creation of superstructures. Establishing direct correlations between crystal chemistry and ion mobility in aluminum-bearing silicate apatites will guide the tailoring of related apatite systems as solid electrolytes.

Tao An, Tom Baikie, Fengxia Wei, Stevin S. Pramana, Martin K. Schreyer, Ross O. Piltz, J. Felix Shin, Christian Kloc, Jun Wei, Peter R. Slater, and Tim J. White\*

*Chem. Mater.*

Crystallographic Correlations with Anisotropic Oxide Ion Conduction in Aluminum-doped Neodymium Silicate Apatite Electrolytes

$\text{Nd}_{(28+x)/3}\text{Al}_x\text{Si}_{6-x}\text{O}_{26}$  crystals grown via the floating-zone method were used to establish baseline performance of these materials as solid electrolytes for operation at intermediate temperatures ( $\leq 700^\circ\text{C}$ ). The location and concentration of oxygen interstitials and neodymium vacancies correlated with anisotropic  $\text{O}^{2-}$  transport. To assess the role of grain boundaries, the oxygen mobility in the large crystals was compared with dense polycrystalline ceramics of similar composition.



## ■ INTRODUCTION

Solid oxide fuel cells (SOFC) are increasingly deployed as fixed and mobile installations for electricity generation due to their high efficiency, chemical and physical stability, and fuel flexibility. Yet the working life of the cells is limited by their high operating temperature that promotes the failure of seals leading to performance degradation.<sup>1</sup> The conventional electrolyte material, yttria-stabilised zirconia (YSZ), only has sufficient  $O^{2-}$  vacancies mobilized to work efficiently at  $>1000^\circ\text{C}$ .<sup>2</sup> For this reason, considerable effort has been devoted to develop alternate ionic conductors for intermediate temperatures ( $\approx 500 - 700^\circ\text{C}$ ), and lanthanoid (*Ln*) silicate and germanate apatites ( $Ln_{9.33}(\text{Si/Ge})_6\text{O}_{26}$ ) have proven to be good candidates for solid electrolyte applications.<sup>3</sup> The ideal crystal chemical formula for the prototypical  $P6_3/m$  apatite-2H polysome is  $[A_4^I][A_6^{II}][(\text{BO}_4)_6][X_2]$  where *A* and *B* are larger and smaller cations and *X* is an anion.<sup>4</sup> These structural elements are arranged as an  $[A_4^I][(\text{BO}_4)_6]$  framework surrounding an  $[A_6^{II}][X_2]$  component (Figure 1). A range of lanthanoid (*Ln*) and alkali earth (*M*) doped oxyapatites have been studied, including stoichiometric  $Ln_8M_2B_6O_{26}$  compounds, cation-deficient  $Ln_{9.33}\square_{0.67}B_6O_{26}$ , and oxygen excess  $Ln_{10-x}M_xB_6O_{27-x/2}$  materials where *Ln* = La, Nd, Sm, Gd and Dy,<sup>3</sup> *M* = Ca, Sr and Ba and *B* = Si and Ge.<sup>5-7</sup> Both neutron diffraction<sup>8</sup> and semi-empirical atomistic simulations<sup>9</sup> show that in  $Ln_{9.33+x}B_6O_{26+1.5x}$  apatites the “excess” oxygen ( $0 < x \leq 0.66$ ) can be introduced in combination with lanthanoids beyond the putative limit of 9.33 atoms per formula unit i.e.  $2\square_A + 3\dot{O} \rightarrow 2Ln^{3+} + 3O^{2-}$ .

In stoichiometric  $La_{10}Ge_6O_{27}$  and non-stoichiometric  $La_9SrGe_6O_{26.5}$  the “interstitial” oxygens are not primarily confined to the  $[La_6^{II}][O_2]$  tunnels, but rather accumulate in the  $[La_4^I][(\text{GeO}_4)_6]$  framework through the conversion of some  $\text{GeO}_4$  tetrahedra to  $\text{GeO}_5$  trigonal bipyramids or square pyramids.<sup>10-12</sup> Furthermore, the insertion of higher valent transition metals (e.g.  $\text{Nb}^{5+}$  and  $\text{W}^{6+}$ )<sup>13</sup> at the Ge site create interstitial contents  $> 1$  oxygen per formula unit, with a maximum for  $La_{10}Ge_{5.5}W_{0.5}O_{27.5}$ .<sup>14</sup>

In the main, silicate apatites have been studied, and while the ion conduction processes are assumed similar to germanates, the literature is ambiguous concerning their crystal chemistry, particularly with respect to *Ln* stoichiometry and interstitial oxide ion positions that control oxygen mobility. These materials are commonly prepared as polycrystalline samples, and more rarely as single crystals using the floating zone method. Solid state,<sup>7-15</sup> sol-gel,<sup>16, 17</sup> hydro-thermal<sup>18</sup> syntheses, and the mechanical milling of constituent oxides<sup>19</sup> can produce monophasic polycrystalline masses. For silicate apatites, a particular problem is the high temperature (typically  $> 1600^\circ\text{C}$ ) required to achieve dense materials for deployment in SOFCs. Sintering at lower temperatures leads to significantly poorer mobility dominated by a grain boundary contribution. Other than prolonged (up to 96h) solid

state sintering, spark plasma sintering and reactive sintering can fabricate dense ( $>90\%$  relative density)  $La_{9.33}\text{Si}_6\text{O}_{26}$  pellets in much shorter times.<sup>20</sup>

Polycrystalline  $Ln_{9.33}\text{Si}_6\text{O}_{26}$  that is stoichiometric in oxygen but cation deficient shows high conductivity, with a small and gradual decrease in performance for the smaller lanthanoids, as constricting the *c*-axis conducting channel inhibits transport. Higher conductivities and lower activation energies are observed as the *Ln* content increases due to the greater abundance of interstitial oxygen up to  $Ln_{9.67}\text{Si}_6\text{O}_{26.5}$ , beyond which secondary phases such as  $Ln_2\text{SiO}_5$  appear. Increasing the *Ln* content (9.33 to 9.67) typically enhances conductivity by an order of magnitude ( $1.1 \times 10^{-4} \text{ Scm}^{-1}$  to  $1.3 \times 10^{-3} \text{ Scm}^{-1}$  at  $500^\circ\text{C}$ ).<sup>8</sup> In the case of  $Ln_{9.33}\text{Si}_6\text{O}_{26}$  single crystals even higher conduction is observed, but with clear anisotropic character, such that conduction parallel to *c* (the direction of the  $[A_4^I][(\text{BO}_4)_6]$  channels) is higher than across the *ab* basal plane (e.g.  $\text{Nd}_{9.33}\text{Si}_6\text{O}_{26}$ ,  $\sigma_c = 6.4 \times 10^{-3} \text{ Scm}^{-1}$ ;  $\sigma_{ab} = 1.3 \times 10^{-3} \text{ Scm}^{-1}$  at  $500^\circ\text{C}$ ). However, the enhancement along *c* (less than one order of magnitude) is not as great as intuitively expected for a crystallographically evident one-dimensional channel. In addition, the activation energies for conduction along *c* and across *ab* are similar, consistent with substantial ionic percolation perpendicular to the channels, possibly mediated by the *Ln* vacancies.

The role of large cation vacancies has received some attention. Studies of both polycrystalline<sup>21, 22</sup> and single crystal<sup>23, 24</sup>  $Ln_{9.33-x}\text{Sr}_{3x/2}\text{Si}_6\text{O}_{26}$  (*Ln* = La and Nd) found that as the Sr content increased, the number of cation vacancies decreases, with the conductivity of stoichiometric  $Ln_8\text{Sr}_2\text{Si}_6\text{O}_{26}$  (*Ln* = La and Nd) invariably low. Similar studies on apatites containing other alkaline earths (Ca, Ba)<sup>22</sup> or even transition metals (Mn)<sup>25</sup> also showed low conductivities and high activation energies.

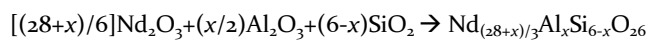
Large ( $> 2\text{mm}$ ) single crystals of certain coloured lanthanoid silicates can be grown with the floating zone method,<sup>26, 27</sup> as these apatites melt congruently.<sup>28, 29</sup> The crystal structures of the lanthanoid silicate apatites were first reported by Felsche<sup>30</sup> from powders, which also contained small single crystals sufficient for preliminary characterisation ( $Ln_{9.33}\square_{0.67}\text{Si}_6\text{O}_{26}$ ,  $\text{LiLn}_9\text{Si}_6\text{O}_{26}$  and  $\text{NaLn}_9\text{Si}_6\text{O}_{26}$ , *Ln* = La – Lu excluding Pm). X-ray precession images of the *Ln* and alkali-*Ln*-analogues were consistent with  $P6_3/m$  or  $P6_3$  (*ool* with  $l \neq 2n$  forbidden at general positions and  $h - k \neq 3n$  for *hkl* at certain special positions), but full structure determinations were not attempted. The high oxide ion conductivity of the lanthanoid silicates was initially recognised by Nakayama et al.<sup>3</sup> (stoichiometry reported as  $Ln_{10}\text{Si}_6\text{O}_{27}$ ; *Ln* = Nd, Sm, Gd, Dy, Y, Ho, Er and Yb) from sintered pellets with the activation energy and conductivity being less favourable for smaller  $Ln^{3+}$  ions. The anisotropy of conduction was determined from single crystals of composition  $Ln_{9.33}(\text{SiO}_4)_6\text{O}_2$  where *Ln* = Pr, Nd and Sm, with oxygen

mobility more than an order of magnitude higher along the *c* axis than perpendicular to it.

We recently reported the successful growth of large neodymium silicate apatite crystals containing a range of Al contents,<sup>31</sup> from sintered polycrystalline rods, using an optical floating zone mirror furnace. A combination of powder X-ray diffraction, electron backscatter diffraction and energy dispersive X-ray spectroscopy, confirmed the high quality of the acicular crystals with extension along the *c* axis and Al at expected concentrations. This article describes single crystal X-ray diffraction of  $\text{Nd}_{(28+x)/3}\text{Al}_x\text{Si}_{6-x}\text{O}_{26}$ , and correlates crystal chemistry with oxide ion transport properties obtained from AC impedance spectroscopy. When the single crystals were subjected to prolonged annealing at 950°C, the oxide ion conductivity deteriorated. Moreover, the conductivity of dense Nd-Si-Al polycrystalline pellets fabricated by spark plasma sintering were comparable to the La-Si-Al analogue, despite the smaller size of the  $\text{Nd}^{3+}$  ions compared to  $\text{La}^{3+}$  that reduces the conducting tunnel diameter. Comparing single crystals and fully dense ceramics of similar composition provides insights into the relative contributions of grain boundaries and defects to oxygen ion mobility.

## ■ EXPERIMENTAL METHODS

**Synthesis.** Polycrystalline  $\text{Nd}_{(28+x)/3}\text{Al}_x\text{Si}_{6-x}\text{O}_{26}$  feed materials for spark plasma sintering and floating zone crystal growth were prepared by conventional solid state reaction. Dried powders of  $\text{Nd}_2\text{O}_3$  (Aldrich, 99.9%),  $\text{SiO}_2$  (Alfa Aesar, 99.9%) and  $\text{Al}_2\text{O}_3$  (Fluka, 99.7%) were manually homogenized in stoichiometric ratios with an agate pestle and mortar. The mixtures were heated at 1200°C for 10h in air, cooled to room temperature and re-ground for 1 hour, followed by sintering in air at 1650°C for 20h. The overall ideal reaction is:



where  $x = 0, 0.5, 1, 1.5$ , and 2.

The floating-zone crystals were confirmed to be monophasic apatites by powder X-ray diffraction (PXRD), with electron backscatter diffraction (EBSD) used to establish preferential growth along the crystallographic *c* axis.<sup>31</sup> Micro-analytical energy dispersive X-ray spectroscopy (EDX) was consistent with the expected elemental concentrations, and polarised optical microscopy showed the crystals were not twinned.

In parallel, dense polycrystalline samples were fabricated by spark plasma sintering (SPS),<sup>32–34</sup> a hot-pressing technique of high heating rate, with a Dr Sinter SPS-825 (SPS Syntex Inc., Japan) apparatus located at the University of New South Wales, Australia. The sintered apatite feedstock was loaded into a  $\phi 20\text{mm}$  graphite die set and uniaxially pressed under vacuum at a constant pressure of 50MPa during the entire process. The temperature was rapidly ramped to 600°C (150°C/min), then to 1400°C (100°C/min), and finally raised to 1500°C in 3 min, at increments of 50°C, 30°C and 20°C in each successive minute. Compression was maintained for 5 min at 1500°C, after which both pressure and power were shut off and the die allowed to cool to ambient over ~2hrs. Finally, the

ceramic pellets were burnt in air (850°C/2h) to remove residual carbon abraded from the die set.

**Powder X-ray Diffraction.** PXRD patterns were collected on a Bruker D8 Advance diffractometer equipped with a Cu X-ray tube operated at 40 kV and 40 mA. The pellets were mounted in a top-loaded holder and data accumulated from 10 – 130° 2 $\theta$  using a step size of 0.02° with a dwell time of 0.6s per step. PXRD data for the single crystals has been described elsewhere.<sup>31</sup> For the SPS samples, the lattice parameters were used to calculate the theoretical density of each pellet for comparison with the geometrical density.

**Scanning Electron Microscopy.** The SPS pellets were polished with SiC paper, followed by a fine silica (0.05 $\mu\text{m}$ ) suspension to achieve a mirror finish, and their backscatter electron (BSE) images collected at 5keV using a JEOL JSM 7600F Field Emission Scanning Electron Microscope (FESEM).

**Single Crystal X-ray Diffraction.** Crystal shards were cleaved from the as-grown and annealed crystal rods. The crystals were mounted on a glass fiber and data collected at 100K using a Bruker SmartApex II three-circle diffractometer with graphite monochromated Mo  $K\alpha$  radiation over the angular range 5 – 65° 2 $\theta$ . SmartApex II software was used for reflection integration, Lorentz polarisation and multi-scan absorption corrections.

The indexed reflections and integrated intensities were treated with Jana 2006<sup>35</sup> using the Superflip<sup>36</sup> structure solution algorithm without further absorption correction. At absolute zero, atoms locate precisely at lattice positions, but for these data collected at 100K, temporally averaged scattering is recorded as a result of thermal vibration. Isotropic modelling of the atomic displacement parameters (ADPs) was first assumed, but certain atoms in apatite are better described with anisotropic motion. VESTA<sup>37</sup> allowed visualisation of the difference Fourier maps in three dimensions, and JANA used to create 2D sections of Fourier difference maps to identify structural disorder. For instance, a site is “split” when positive electron density is concentrated about a high symmetry lattice position in the difference Fourier map. In these cases, the structure may be better described by lower symmetry or as a superstructure. Negative electron density, on the other hand, indicates anomalously high scattering, and therefore, site chemistry adjusted with lower atomic number species or reduced occupancy.

**AC Impedance Spectroscopy.** Conductivity measurements were carried out on the SPS pellets, and discs cut from the as-grown crystals with approximate dimensions 5 × 5 × 3 mm. Opposing faces of the discs were coated with gold paste and then heated at 700°C for 1 h to ensure bonding. Conductivity measurements were made in air from 370°C to 860°C using AC impedance spectroscopy (Hewlett Packard 4182A impedance analyser, frequency range 10 Hz to 13 MHz, applied voltage of 0.1V). Data were collected from the polycrystalline pellets and single crystals with nominal compositions  $\text{Nd}_{9.33}\text{Si}_6\text{O}_{26}$ ,  $\text{Nd}_{9.5}\text{Si}_{5.5}\text{Al}_{0.5}\text{O}_{26}$ ,  $\text{Nd}_{9.67}\text{Si}_5\text{AlO}_{26}$ ,  $\text{Nd}_{9.83}\text{Si}_{4.5}\text{Al}_{1.5}\text{O}_{26}$  and  $\text{Nd}_{10}\text{Si}_4\text{Al}_2\text{O}_{26}$  (polycrystalline pellet only), and also from

$\text{Nd}_{9.33}\text{Si}_6\text{O}_{26}$  and  $\text{Nd}_{9.5}\text{Si}_{5.5}\text{Al}_{0.5}\text{O}_{26}$  single crystals annealed at 950°C for 1, 2 and 3 months to investigate long term stability and changes in conductivity.

## ■ RESULTS

**Dense Polycrystalline  $\text{Nd}_{(28+x)/3}\text{Al}_x\text{Si}_{6-x}\text{O}_{26}$  Apatites Fabricated by SPS.** Rietveld analysis<sup>38</sup> of the PXRD data showed that pellets with the compositions  $x = 0, 1$ , and  $1.5$  were monophasic apatite; while the  $x = 0.5$  pellet has apatite as the major phase (90wt%) and  $\text{Nd}_2\text{SiO}_5$  as the secondary phase (10wt%). The  $x = 2.0$  ceramic has 95wt% apatite,  $\text{NdAlO}_3$  (2wt%) and  $\text{Nd}_2\text{O}_3$  (3wt%) (Figure 2). While all the samples have over 90% relative density, those for  $x \geq 1.0$  were particularly well consolidated (Table 1).

Figure 3 shows the BSE image of a high density pellet of  $\text{Nd}_{9.67}\text{AlSi}_5\text{O}_{26}$  with a few cracks and grain boundaries chemically indistinguishable from the bulk. The top right region of this image contains some contrast variation, that may be due to a small change in orientation, as energy dispersive X-ray spectroscopy (EDX) could not differentiate the composition. All SPS pellet compositions displayed similar microstructures.

As described previously, Al-doping removes  $\text{Nd}^{3+}$  vacancies and makes O interstitials less abundant, but also dilates the unit cell which reduces steric hindrances to oxygen transport.<sup>31</sup> The conductivities of the  $\text{Nd}_{(28+x)/3}\text{Al}_x\text{Si}_{6-x}\text{O}_{26}$  pellets with  $x = 0, 0.5, 1.5$  and  $2.0$  behave similarly to the La-Si-Al analogue,<sup>5</sup> where the bulk conductivities of the intermediate compositions ( $x = 0.5$  and  $1.5$ ) are significantly greater than the Al-free ( $x = 0$ ) and highly doped ( $x = 2.0$ ) apatites (Figure 4). This suggests maximum conductivity is achieved when the partial removal of  $\text{Nd}^{3+}$  vacancies and O interstitials are more than offset by steric enhancements that favour mobility. However, in the case of  $x = 2.0$ , with the least steric hindrance, there are few mobile oxygen, and the conductivity is similar to that of the undoped pellet ( $x = 0$ ).

**As-grown Single Crystals.** All crystals selected for analysis ( $x \leq 1.5$ ) gave systematic absences consistent with the hexagonal space group  $P6_3/m$ , in agreement with previous reports,<sup>39</sup> and were free of  $\text{NdAlO}_3$  as a secondary phase. For the Al-free crystal, isotropic ADPs were initially applied to all atomic sites, leading to a poor goodness of fit (GOF) (Figure 5). In particular, the Nd(1) site is surrounded by dumbbell-shaped (001) in-plane negative electron density with positive electron density above and below along [001] consistent with an anisotropic atomic distribution. A harmonic model for ADPs reduced the negative electron density around the Nd(1), but the positive electron density near the O(3) site remained. To account for this, the O(3) site was split and gave satisfactory fitting. Finally, to eliminate the negative electron density at Nd(1), the site occupancy was refined. For the Al-doped crystals, the same strategy was applied with the Si/Al ratio fixed at the expected value. However, these Al-doped samples show poorer fitting to the  $P6_3/m$  model (Figure 6), with difference Fourier map features suggesting static site splitting, in contrast to those of the undoped single

crystal at room and elevated temperatures, that may be ascribed to anharmonic motion of the  $\text{Nd}^{40}$ . Tables 2 and 3 show the refined atomic positions and displacement parameters respectively, with the bond valence sums (BVS)<sup>41</sup> in Table 4. From the refined Nd(1) occupancies, the compositions of the crystals can be calculated.

The as-grown crystals unambiguously show (Figure 7 and Table 5) that conductivity parallel with the  $c$  direction is approximately one order of magnitude higher than in the  $ab$  basal plane. In addition, the activation energies for conduction for both the  $c$  and  $ab$  directions are similar, so although the main conduction pathway is along the channel there is significant perpendicular migration.

For higher  $x$  there is a noticeable reduction in the anisotropy between the  $ab$  and  $c$  axes, which suggests the vacancies have a detrimental effect on basal plane conductivity (Figure 7). As the Al concentration increases, the conductivity decreases with a corresponding increase in the activation energy (Figure 8 and Table 6), and there is a smaller difference between the high and low temperature activation energies. The corresponding  $ab$  basal plane conductivities (Figure 9 and Table 7) first increase to  $x = 1.0$ , then slightly decrease for  $x = 1.5$ , but both have a higher basal plane conductivity than the undoped material.

**Annealed Single Crystals.** A portion of the as-grown  $x = 0$  and  $x = 0.5$  crystals were annealed in air, at 950°C for 3 months. At monthly intervals, the crystals were removed from the furnace for impedance spectrometry (Figures 10 and 11). For  $x = 0$ , annealing for 1 month reduced the apparent grain boundary contribution and the overall conductivity. After 2 months annealing these changes were more evident with the second component disappearing entirely. After 3 months, the conductivity was approximately two orders of magnitude less than the as-grown single crystal; further annealing did not lead to a measurable change, and the differential between high and low temperature activation energies ultimately disappears along with the second semicircle (Table 8).

The as-prepared  $x = 0.5$  crystal also showed a second component in the impedance plot notionally interpreted as a grain boundary contribution, that together with bulk conductivity, was reduced after one month annealing at 950°C (Table 9). Similar to the  $x = 0$  crystal the smaller semicircle disappeared following 2 months annealing, but distinctively, a new component appeared in the impedance plots. Further annealing did not alter the impedance features. It is probable that the appearance of the new component is due to phase segregation in the crystal, as subsequent PXRD revealed additional reflections inconsistent with apatite.

Single crystal X-ray diffraction of the  $x = 0$  and  $0.5$  samples after 3-month annealing revealed significant changes. Using the same  $P6_3/m$  model, their refined compositions were much closer to the nominal ones (Table 10) and the difference Fourier maps contain less residual scattering density (Figure 12).

## ■ DISCUSSION

BVS found that except for the trivalent  $\text{Al}^{3+}$  ions that were greatly overbonded, all other atoms were near their formal valencies confirming their crystallographic placements (Table 4). Both Nd(1) (BVS = 2.86 – 2.97) and Nd(2) (BVS = 2.88 – 2.91) are somewhat underbonded, i.e. the Nd-O bonds were stretched, and for the former, might be expected given the larger ADPs and site splitting. For Si, the partial incorporation of Al in the tetrahedral site causes  $\text{Si}^{4+}$  to be underbonded, due to stretching of Si-O average bonds, as  $\text{Al}^{3+}$  is 50% larger than  $\text{Si}^{4+}$ .<sup>42</sup> On the other hand, while O atoms are generally overbonded, O(3) is underbonded for all crystals, as the latter is a split site, indicative of mobile oxygen.

While the GOF and R-values of the undoped crystal are acceptable, Si became progressively more underbonded as Al content increased. This observation would also be consistent with variation in B-O co-ordination, as suggested in earlier magic angle spinning nuclear magnetic resonance (MAS NMR) Si spectroscopy where  $\text{SiO}_5$  and  $\text{SiO}_6$  entities were detected.<sup>8</sup> Furthermore, the difference Fourier maps (Figure 6) show substantial discrepancies around the Nd (1) site. Rocking beam X-ray diffraction of the single crystals (Figure 13) yield convoluted peaks consistent with lower symmetry, and future high energy synchrotron X-ray diffraction enabling the exploration of more reciprocal space may recognize long range order and confirm the space group. Evidentially, it is important to confirm the O positions, especially the partially occupied sites, and to this end neutron diffraction of the crystals will locate interstitials and deduce the  $\text{O}^{2-}$  transport routes and conduction mechanisms as already used to completely describe  $\text{La}_{10}[(\text{GeO}_4)_5(\text{GeO}_5)]\text{O}_2$ .<sup>8</sup>

Higher Nd(1) cation vacancy concentrations are detrimental to the *ab* basal plane conductivity. Although  $x = 1.5$  has fewer vacancies than  $x = 1.0$  the slightly lower conductivity for the former is probably related by the lower oxygen interstitial concentration; three interstitial oxygens are removed for every two Nd vacancies created. Conversely, decreasing cation vacancies degrades interstitial transport and lowers conductivity along the *c* axis. Overall, Al increases the conductivity in the *ab* basal plane, but decreases the conductivity along the *c* axis, and on balance intermediate Al levels ( $0.5 \leq x \leq 1.5$ ) lead to enhanced oxygen mobility.

For the annealed crystals, bulk conductivity is least affected for  $x = 0.5$  and the resistance to thermal treatment might be exploited to extend the operating life of a fuel cell. With  $x = 0.5$  there is an initial reduction in activation energy with annealing, which becomes more evident with prolonged annealing, and the temperature dependence of activation energies is removed with increased annealing time.

This work shows for the first time a “grain boundary contribution” to the conductivity in single crystals; this additional feature is only observed along the *c* direction but not in the *a-b* basal plane. The conductivity plot shows that when the [001] “grain boundary” conductivity exceeds  $\langle 100 \rangle / \langle 110 \rangle$  there is an accompanying enhancement to the *c* axis conductivity, evidenced by a small departure from linearity. Once this contribution is compa-

rable to the *c* axis bulk component the enhancement disappears and reverts to the original linear trend. A comparison of the high and low temperature activation energies for the *ab* and *c* directions (Table 5) shows that the activation energy for the basal plane is essentially unchanged over the whole temperature regime but the “grain boundary” significantly reduces *c* axis activation energy at high temperature.

Polarised optical microscopy and electron backscattered diffraction (EBSD) found the single crystals to consist of a single grain,<sup>31</sup> and so, the “grain boundary” component in the impedance plots requires explanation. In addition, the changes to the second semicircle of the AC impedance spectra occur at a relatively low temperature of 950°C, whereas much higher temperatures of >1500°C would typically be required to modify a grain boundary contribution. It is suggested the crystals initially contain a high concentration of conducting defects (i.e. oxide ion interstitials). There must however be small regions where there is partial blocking of the conduction, for example interfaces between regions of high and low interstitial content (e.g.  $\text{Nd}_{9.67}\text{Si}_6\text{O}_{26.5}$  and  $\text{Nd}_{9.33}\text{Si}_6\text{O}_{26}$ ). On annealing, Nd redistribution and homogenization removes interfaces, lowers the bulk conductivity and eliminates the second semicircle. Consequently, single crystal X-ray structure determinations after 3-month annealing were of higher quality and the experimental and nominal compositions are in better agreement. One explanation is that  $\text{Si}_2\text{O}_7$  groups are present in the as-prepared crystals, as suggested from <sup>19</sup>Si NMR studies of polycrystalline La containing analogues,<sup>8</sup> and are associated with the stabilization of Nd(1) vacancies through the creation of the defect cages proposed by Baikie et al.<sup>4</sup> that partially disrupt the conduction pathway. During annealing, the mobile interstitial oxide ions react with  $\text{Si}_2\text{O}_7$  i.e.  $\text{O}^{2-} + \text{Si}_2\text{O}_7^{6-} \rightarrow 2\text{SiO}_4^{4-}$ , lowering bulk conductivity. Furthermore, the as-prepared single crystals apparently contain compositionally discrete domains with more or less interstitial oxygen, and the interfaces between these, give rise to the pseudo grain boundary semicircle in the impedance plots. As the crystals used in this study contain magnetic  $\text{Nd}^{3+}$  rather than  $\text{La}^{3+}$ , it was not possible to use MAS NMR to directly confirm the presence of  $\text{Si}_2\text{O}_7$  units.

## ■ CONCLUSION

Dense polycrystalline  $\text{Nd}_{(28+x)/3}\text{Al}_x\text{Si}_{6-x}\text{O}_{26}$  ceramic pellets were fabricated by SPS and large single crystals of comparable composition were prepared using the floating zone method. Doping with Al generally enhanced conductivity (for  $0.5 \leq x \leq 1.5$ ) but for  $x = 2.0$  the Nd(1) site is fully occupied and interstitial oxygens are removed which eliminates oxygen mobility. Anisotropic conductivity was measured for the single crystals along [001] and across the *ab* basal plane. It was found that for  $x = 0.5, 1.0$  and  $1.5$ , Al-doping decreases conductivity along the *c* axis, but increases conductivity perpendicular to it, due to the negative factor of fewer oxygen interstitials being more than offset by unit cell dilation sterically favors oxygen transport. Notably, the second component in the impedance measurements of the single crystals disappeared

after prolonged annealing. This was accompanied by a decrease in conductivity due to the elimination of beneficial  $\text{Si}_2\text{O}_7$  defects, that increase the concentration of mobile  $\text{O}^{2-}$  through stabilization of  $\text{SiO}_4/\text{SiO}_5$  cluster, and the concurrent removal of interfaces separating domains of distinct oxygen content. This interpretation is consistent with the higher quality structure determinations after annealing and the superior agreement of experimental and bulk compositions. Also, the rocking curves showed overlapped peaks, suggesting the local distortion of the lattice.

For the Al-free crystal, structure determination confirmed  $P6_3/m$ . For the Al-doped crystals the BVS for Si shows significant underbonding, as  $\text{Al}^{3+}$  dilates the average size of the  $\text{Si}/\text{AlO}_4$  tetrahedron, and for the aluminous apatites, difference Fourier maps revealed Nd(1) site splitting, as well as positive electron density around Nd(2) sites. Therefore, the  $P6_3/m$  model of undoped neodymium silicate cannot completely describe the Al-doped materials and further study of synchrotron and neutron diffraction will be necessary to more completely describe those structures.

The appearance of Nd-rich and Nd-poor apatite domains that enhance overall conductivity has not been previously recognized, although the possible appearance of  $\text{Si}_2\text{O}_7$  at the interface regions was known. The present study shows that extended exposure to higher temperatures, as would be experienced during SOFC operation, may ultimately remove these apatite domains and reduce performance. The observation that light Al-doping enhances thermal stability, and simultaneously expands the lattice to enhance oxygen mobility is therefore of interest in designing durable apatite electrolytes.

## ■ ASSOCIATED CONTENT

Single crystal X-ray diffraction data in Crystallographic Information File (CIF) format. This material is available free of charge via the Internet at <http://pubs.acs.org>.

## AUTHOR INFORMATION

### Corresponding Author

\* Email: [tjwhite@ntu.edu.sg](mailto:tjwhite@ntu.edu.sg).

### Notes

The authors declare no competing financial interest.

## ACKNOWLEDGMENT

We would like to acknowledge Agency for Science, Technology and Research (A\*STAR) PSF grant 082 101 0021 'Optimization of Oxygen Sublattices in Solid Oxide Fuel Cell Apatite Electrolytes' for funding the work and Ministry of Education (MOE) Tier 2 grant T208B1212 for enabling the purchase of a single crystal X-ray diffractometer. We would also like to thank Prof Sean Li and University of New South Wales for access of their SPS apparatus.



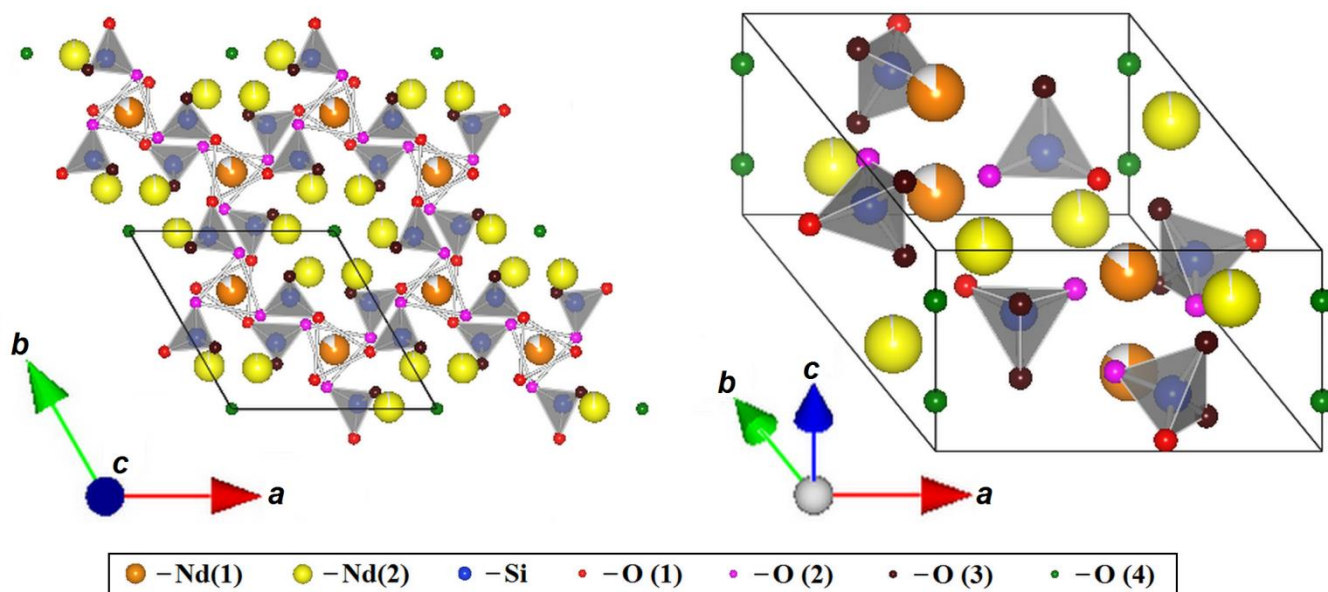


**Figure 1.** The rare earth silicate apatite  $\text{Nd}_{9.33}\text{Si}_6\text{O}_{26}$ <sup>39</sup> is best described by the structural formula  $[\text{Nd}_{3.33}^{I}\square_{0.67}][\text{Nd}_6^{II}][(\text{SiO}_4)_6][\text{O}_2]$ . The  $\text{Nd}(1)$  atoms locate at the framework sites with  $4f$  symmetry and their occupancy is represented by the filled area of the sphere (right). Each  $\text{Si}$  atom ( $6h$ ) is bonded to one  $\text{O}(1)$  atom ( $6h$ ), one  $\text{O}(2)$  atom ( $6h$ ) and two  $\text{O}(3)$  atoms ( $12i$ ) to form a rigid  $\text{SiO}_4$  tetrahedron (left). Per unit cell six of  $\text{SiO}_4$  tetrahedra and 3.33  $\text{Nd}(1)$  atoms form the framework that encloses the six  $\text{Nd}(2)$  atoms ( $6h$ ), which in turn surround the remaining two  $\text{O}(4)$  atoms ( $2a$ ) located along the  $c$  axis. A channel is formed when these layers are stacked on top of one another.

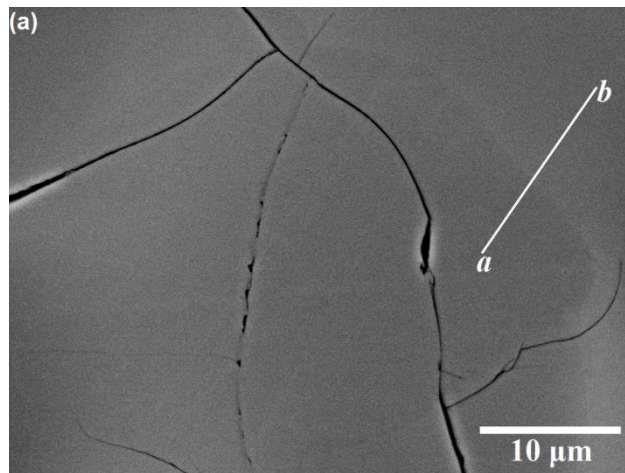
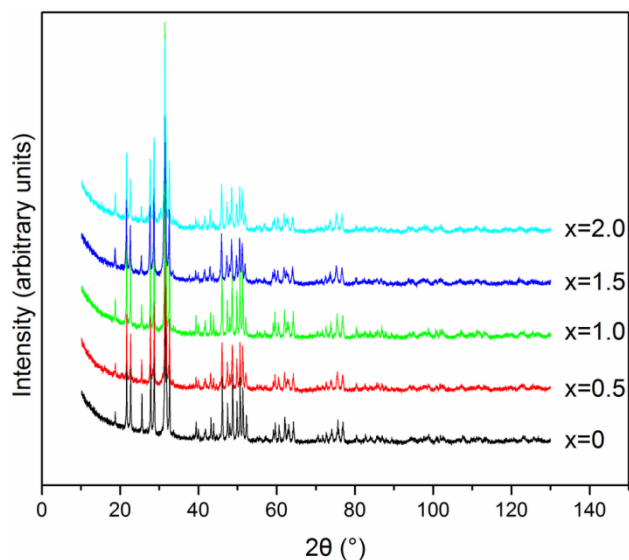


**Figure 2.** PXRD patterns for dense polycrystalline  $\text{Nd}_{(28+x)/3}\text{Al}_x\text{Si}_{6-x}\text{O}_{26}$  pellets with  $x = 0, 0.5, 1.0, 1.5$  and  $2.0$  fabricated by SPS.



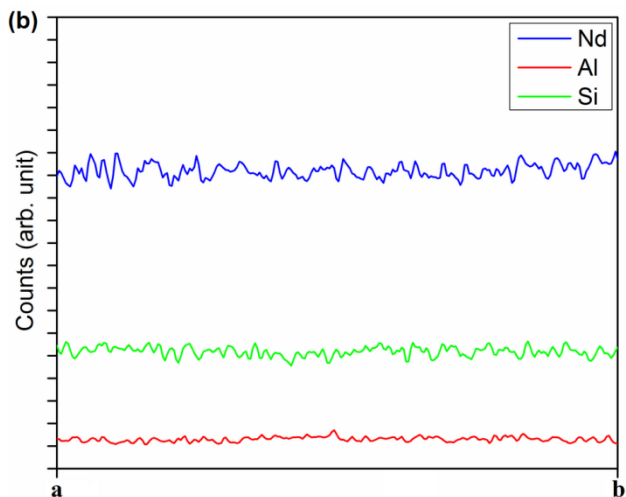


**Figure 3.** (a) A representative backscattered electron (BSE) image of the  $\text{Nd}_{9.67}\text{AlSi}_5\text{O}_{26}$  pellet. A grain boundary was observed separating two regions with slightly different brightness. (b) An elemental line scan along the line *a-b* across this grain boundary could not detect a change in composition.

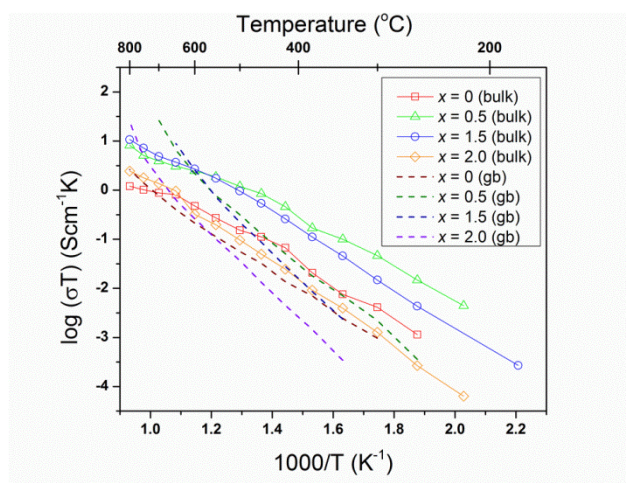


**Figure 4.** Ionic conductivity for the dense polycrystalline  $\text{Nd}_{(28+x)/3}\text{Al}_x\text{Si}_{6-x}\text{O}_{26}$  pellets with  $x = 0, 0.5, 1.5$  and  $2.0$ .

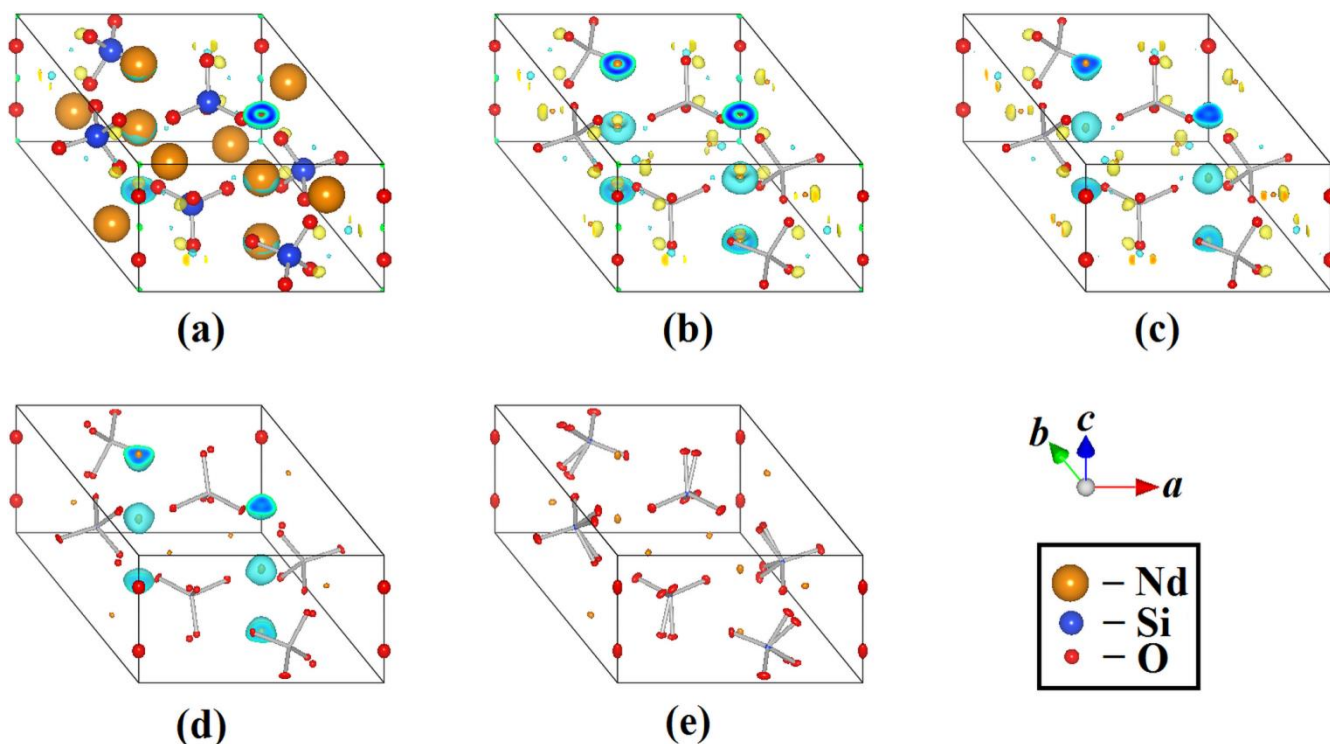


**Figure 5.** A series of 3D visualizations of electron density difference Fourier maps for the undoped single crystal showing the refinement methodology. Isotropic ADPs lead to (a) significant excess scattering and (b) ellipsoidal electron distributions with positive (yellow colored) and negative (blue colored) electron densities around the atomic sites. Subsequent refinement with (c) an anisotropic model for displacement parameters, (d) splitting the O(3) sites and (e) refining occupancy at Nd(1) sites progressively improves the GOF.

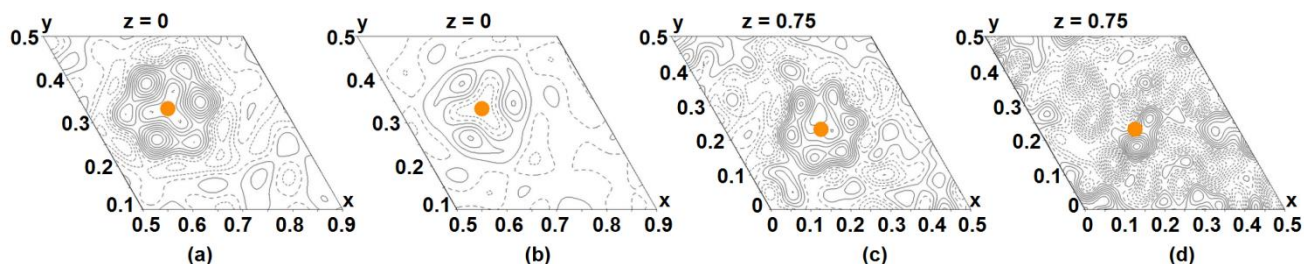


**Figure 6.** The difference Fourier maps of as-prepared Al-doped crystals in  $P6_3/m$  near (a, b) the Nd(1) framework site and (c, d) the Nd(2) tunnel site. The step size of the positive (solid line) and negative (dotted line) contours is 0.5 electrons and Nd atom is represented by an orange sphere. Both (a) the  $x = 0.5$  and (b) the  $x = 1.5$  crystals have clear splitting of the Nd(1) sites, which cannot be accounted for with a harmonic thermal vibration model. Surrounding the Nd(2) sites, (c) the  $x = 0.5$  crystal has positive electron densities while (d) the  $x = 1.0$  crystal shows negative density, that cannot be satisfactorily modeled. The discrepancies arise from the presence of domains with different oxygen contents accommodated through mixing of  $\text{SiO}_4$ ,  $\text{SiO}_5$  and  $\text{Si}_2\text{O}_7$  entities.

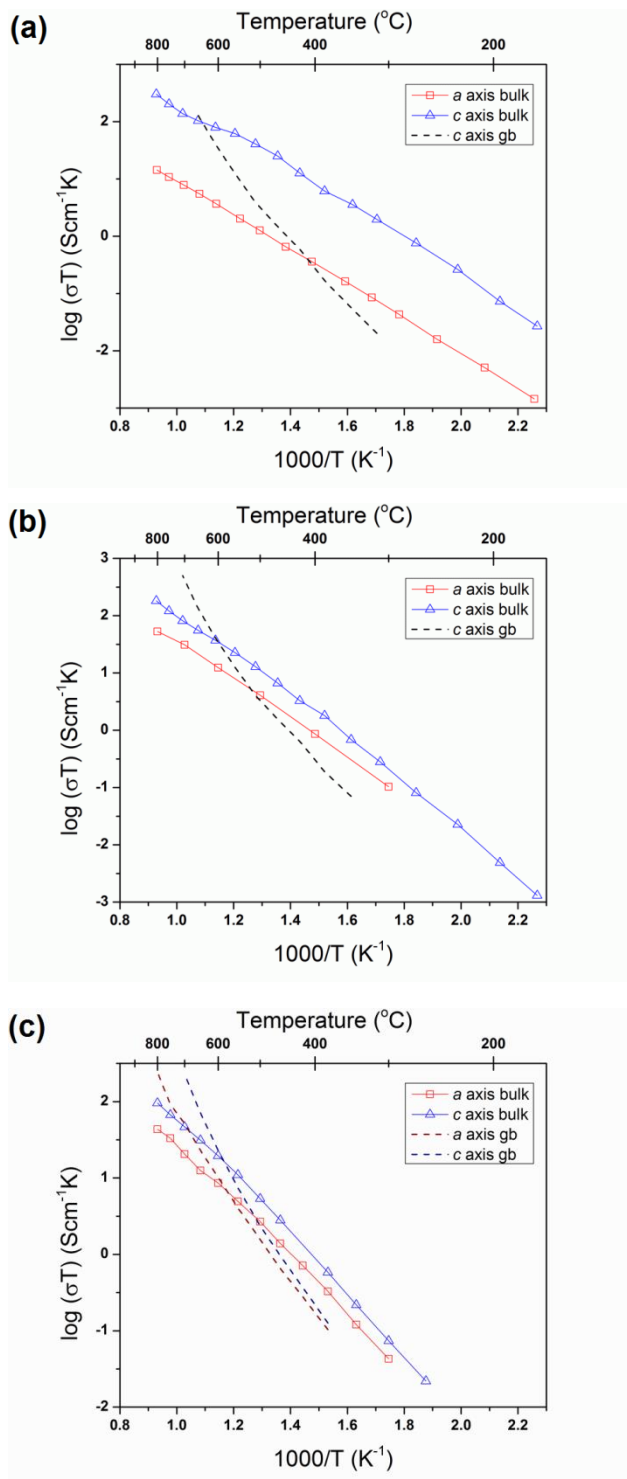


**Figure 7.** The conductivity for the as-prepared single crystals with compositions (a)  $x = 0$  (b)  $x = 1$  (c)  $x = 1.5$  across the  $ab$  basal plane and along the crystallographic  $c$  axes. Also indicated in the plot is the pseudo grain boundary (gb) contribution to the conductivity.

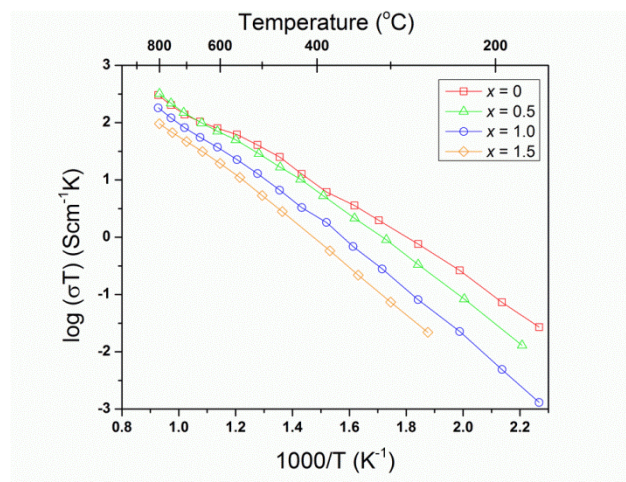


**Figure 8.** Comparison of the conductivities along the  $c$  axis for the as-prepared crystals with compositions for  $x = 0, 0.5, 1.0$  and  $1.5$ .

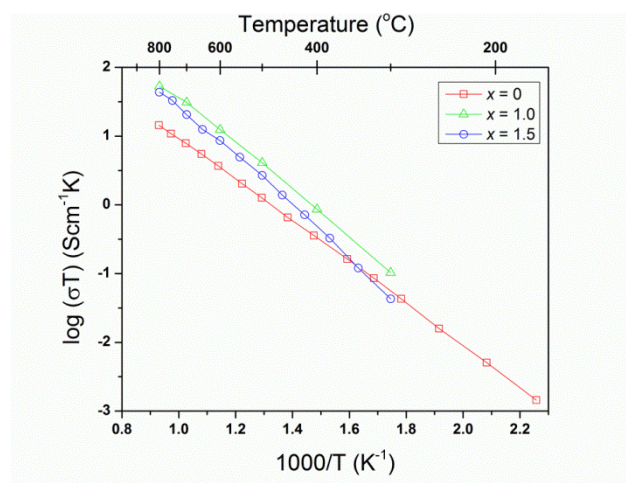


**Figure 9.** Comparison of the  $ab$  basal plane conductivities for the as-prepared crystals with compositions for  $x = 0, 1.0$  and  $1.5$ .



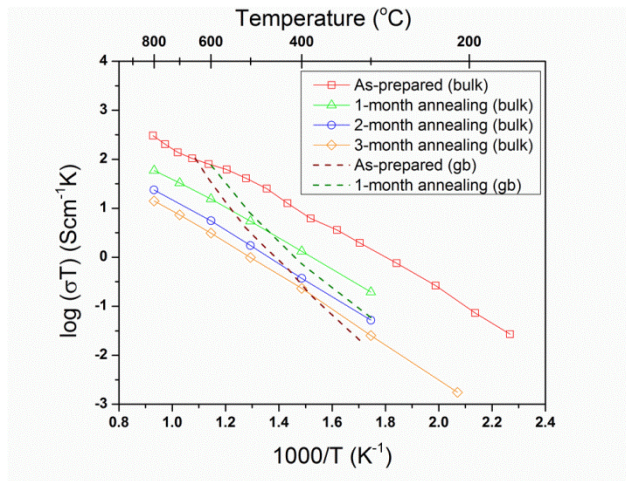


**Figure 10.** Changes in *c*-axis conductivity for the undoped apatite crystals following annealing at 850°C for various times. Also shown are the apparent “grain boundary” contributions to the conductivity from the as-prepared and 1-month annealed crystal, which subsequently disappeared with further annealing.

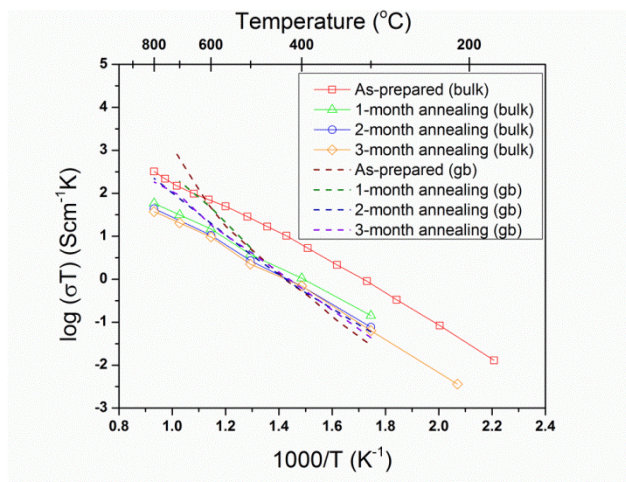


**Figure 11.** Changes in *c*-axis conductivity for the Al-doped apatite crystal (for  $x = 0.5$ ) following annealing at 850°C. Also included are the pseudo grain boundary contributions from the as-prepared and 1-month annealed crystal, that disappeared with annealing. Longer annealing ( $> 1$  month) lead to a third component in the conductivity plots (2-3 month annealing grain boundary) ascribed to phase separation as confirmed by PXRD.

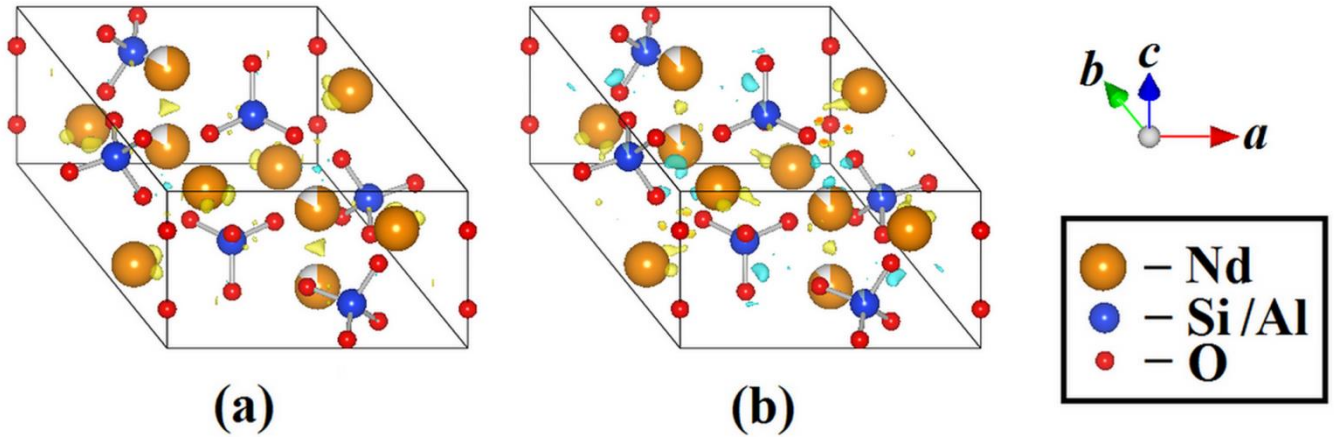


**Figure 12.** The 3D difference Fourier maps for crystals with (a)  $x = 0$  and (b)  $x = 0.5$  after 3-month annealing. Similar to the crystals before annealing, residual densities can be observed surrounding the Nd (2) site. For the undoped crystal, there are positive electron densities with triangular shape (yellow-colored) between each pair of Nd (1) sites. For the  $x = 0.5$  crystal, the differences are less significant but there is clear splitting of the Nd (1) sites, with both positive and negative densities observed.

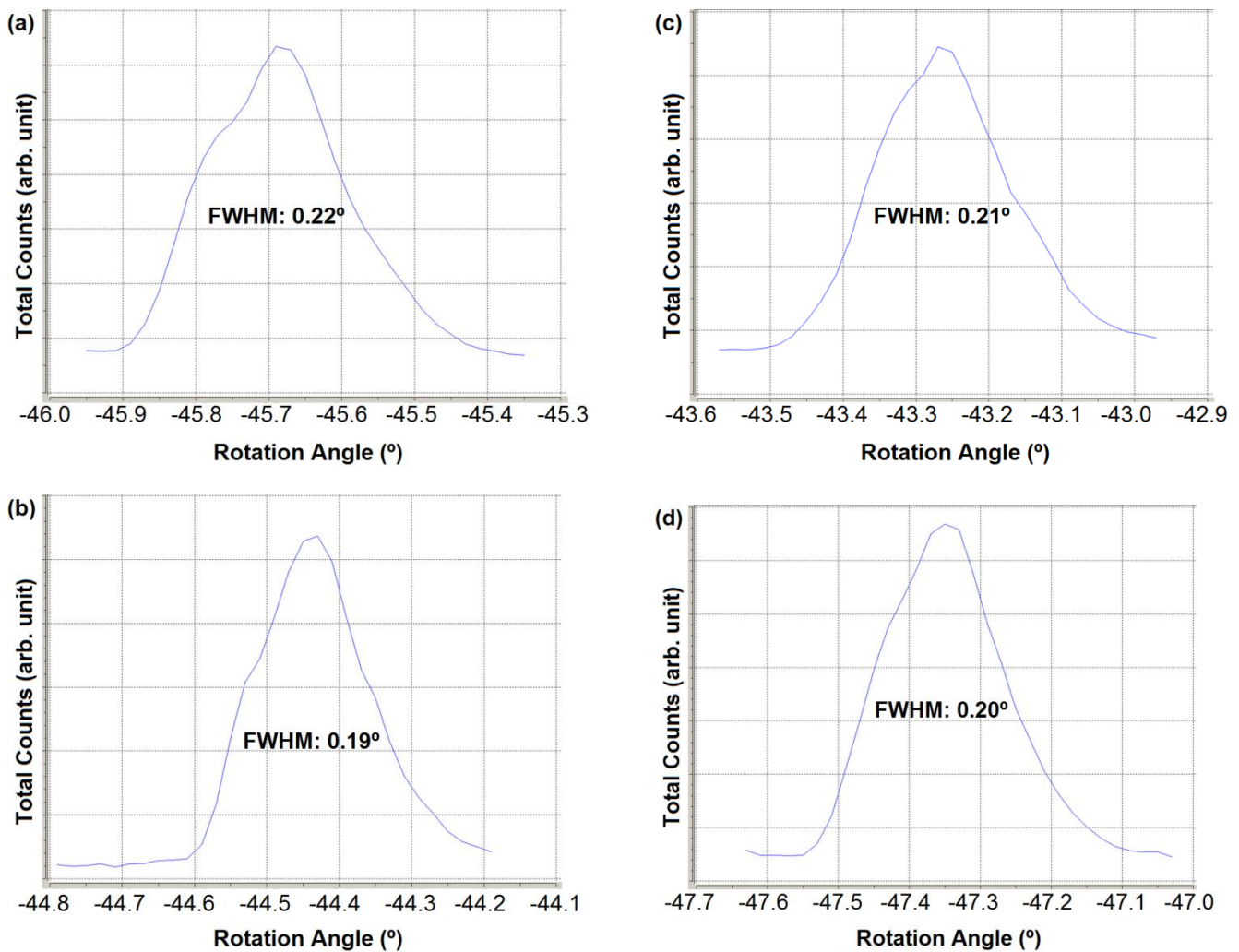


**Figure 13.** X-ray rocking curves about the  $(3\ 5\ 1)$  reflection of crystals with (a)  $x = 0$  (b)  $x = 0.5$  (c)  $x = 1.0$  and (d)  $x = 1.5$ . While the FWHM of  $0.19^\circ$ – $0.22^\circ$  are comparable to previously reported Nd oxide single crystals with good quality,<sup>43</sup> each curve clearly consists of two overlapping peaks, and would be consistent with the presence of domains of different oxygen content as implied by AC impedance spectroscopy.

**Table 1.** Refined unit cell parameters and relative densities of polycrystalline  $\text{Nd}_{(28+x)/3}\text{Al}_x\text{Si}_{6-x}\text{O}_{26}$  samples for  $x = 0, 0.5, 1.0, 1.5$  and  $2.0$ . The relative density calculation took account of the abundance of minor phases when present.

Nominal formula	$\text{Nd}_{9.33}\text{Si}_6\text{O}_{26}$	$\text{Nd}_{9.50}\text{Al}_{0.5}\text{Si}_{5.5}\text{O}_{26}$	$\text{Nd}_{9.67}\text{AlSi}_5\text{O}_{26}$	$\text{Nd}_{9.83}\text{Al}_{1.5}\text{Si}_{4.5}\text{O}_{26}$	$\text{Nd}_{10}\text{Al}_2\text{Si}_4\text{O}_{26}$
$R_{\text{wp}}$ (%)	4.66	4.79	4.41	4.41	5.84
$R_p$ (%)	3.54	3.63	3.39	3.40	4.50
$\chi^2$	1.48	1.43	1.46	1.49	1.28
$R_B$ (%)	1.91	2.57	2.10	1.46	1.11
$R_{\text{exp}}$ (%)	3.15	3.34	3.01	2.96	4.56
$a$ (Å)	9.5761(2)	9.5761(8)	9.5806(7)	9.596(2)	9.6044(8)
$c$ (Å)	7.0282(3)	7.0468(6)	7.0532(5)	7.073(2)	7.0769(6)
Volume (Å <sup>3</sup> )	558.15(3)	559.6(1)	560.67(9)	564.0(3)	565.4(1)
Theoretical density (g/cm <sup>3</sup> )	5.75(1)	5.82(1)	5.844(9)	5.92(1)	5.87(2)
Pellet mass (g)	5.58	3.93	4.27	3.97	7.87
Diameter (mm)	20.12	20.01	20.24	20.11	20.1
Thickness (mm)	3.22	2.38	2.32	2.19	4.28
Pellet density (g/cm <sup>3</sup> )	5.45	5.25	5.72	5.71	5.80
Secondary Phase (wt%)	None	$\text{Nd}_2\text{SiO}_5$ 10	None	None	$\text{NdAlO}_3, \text{Nd}_2\text{O}_3$ 2, 3
Relative density (%)	94.8	90.0*	97.9	96.5	98.1*

\*For pellets containing secondary phase(s), the same relative density (i.e. the ratio of the theoretical density to the geometrical density after the compaction) was assumed for all phases, and calculated by dividing the total theoretical volume (sum-mation of theoretical volume of each phase) by the geometrical volume measured from the pellet.

**Table 2.** Atomic positions from single crystal X-ray diffraction of  $\text{Nd}_{(28+x)/3}\text{Al}_x\text{Si}_{6-x}\text{O}_{26}$  for  $x = 0, 0.5, 1.0$  and  $1.5$ .

Nominal $x$	0	0.5	1.0	1.5
Refined composition	$\text{Nd}_{9.468(8)}\text{Si}_6\text{O}_{26.20(1)}$	$\text{Nd}_{9.77(2)}\text{Al}_{0.5}\text{Si}_{5.5}\text{O}_{26.41(3)}$	$\text{Nd}_{9.78(2)}\text{AlSi}_5\text{O}_{26.17(3)}$	$\text{Nd}_{9.92(2)}\text{Al}_{1.5}\text{Si}_{4.5}\text{O}_{26.13(3)}$
GOF	1.82	3.22	3.20	3.04
R (%)	2.22	4.83	3.72	2.76
$R_w$ (%)	5.88	12.22	10.72	8.75
$\text{Nd}(1)$ , $4f$ , $(1/3\ 2/3\ z)$				
z	-0.00079(4)	0.00001(9)	-0.00006(8)	0.00006(7)
Occupancy	0.867(2)	0.943(5)	0.945(5)	0.981(4)
$\text{Nd}(2)$ , $6h$ , $(x\ y\ 1/4)$				
x	0.01014(2)	0.00937(6)	0.00934(5)	0.00842(4)
y	0.24006(2)	0.24130(6)	0.24123(5)	0.24115(4)
$\text{Si/Al}$ , $6h$ , $(x\ y\ 1/4)$				
x	0.4016(1)	0.4016(3)	0.4014(3)	0.4019(2)
y	0.3725(3)	0.3725(3)	0.3726(3)	0.3727(2)
$\text{O}(1)$ , $6h$ , $(x\ y\ 1/4)$				
x	0.3216(4)	0.320(1)	0.3184(9)	0.3198(7)
y	0.4866(4)	0.487(1)	0.4860(8)	0.4881(7)
$\text{O}(2)$ , $6h$ , $(x\ y\ 1/4)$				
x	0.5970(3)	0.6008(9)	0.6000(8)	0.6022(7)
y	0.4734(4)	0.4746(9)	0.4739(7)	0.4737(6)
$\text{O}(3)$ , $12i$ , $(x\ y\ z)$				
Occupancy	0.79(2)	-	-	-
x	0.352(1)	0.3464(8)	0.3458(7)	0.3465(6)
y	0.2546(4)	0.2531(7)	0.2533(6)	0.2527(5)
z	0.0626(7)	0.0634(7)	0.0630(7)	0.0622(6)
$\text{O}'(3)$ , $12i$ , $(x\ y\ z)$				
Occupancy	0.21(2)	-	-	-
x	0.301(3)	-	-	-
y	0.244(2)	-	-	-
z	0.088(3)	-	-	-
$\text{O}(4)$ , $2a$ , $(0\ 0\ 1/4)$				



**Table 3.** Atomic displacement parameters (ADP) from single crystal X-ray diffraction of  $\text{Nd}_{(28+x)/3}\text{Al}_x\text{Si}_{6-x}\text{O}_{26}$  for  $x = 0, 0.5, 1.0$  and  $1.5$ .

Nominal $x$	0	0.5	1.0	1.5
Refined composition	$\text{Nd}_{9.464(8)}\text{Si}_6\text{O}_{26.20(1)}$	$\text{Nd}_{9.77(2)}\text{Al}_{0.5}\text{Si}_{5.5}\text{O}_{26.41(3)}$	$\text{Nd}_{9.78(2)}\text{AlSi}_5\text{O}_{26.17(3)}$	$\text{Nd}_{9.92(2)}\text{Al}_{1.5}\text{Si}_{4.5}\text{O}_{26.13(3)}$
<b>Nd (1), <math>4f</math>, <math>(1/3 \ 2/3 \ z)</math></b>				
$U_{11}$	0.0081(2)	0.0149(4)	0.0092(3)	0.0102(2)
$U_{33}$	0.0202(2)	0.0058(4)	0.0101(4)	0.0049(3)
<b>Nd (2), <math>6h</math>, <math>(x \ y \ 1/4)</math></b>				
$U_{11}$	0.0063(1)	0.0087(3)	0.0029(3)	0.0049(2)
$U_{22}$	0.0079(2)	0.0086(3)	0.0026(3)	0.0042(2)
$U_{33}$	0.0075(2)	0.0051(3)	0.0091(3)	0.0063(3)
$U_{12}$	0.00248(8)	0.0033(2)	0.0004(2)	0.0017(2)
<b>Si/Al, <math>6h</math>, <math>(x \ y \ 1/4)</math></b>				
$U_{11}$	0.0087(4)	0.010(1)	0.0017(9)	0.0036(8)
$U_{22}$	0.0075(4)	0.009(1)	0.0023(9)	0.0044(8)
$U_{33}$	0.0054(4)	0.004(1)	0.007(1)	0.0043(9)
$U_{12}$	0.0053(4)	0.005(1)	0.0011(8)	0.0019(7)
<b>O (1), <math>6h</math>, <math>(x \ y \ 1/4)</math></b>				
$U_{11}$	0.028(2)	0.032(5)	0.019(3)	0.016(3)
$U_{22}$	0.024(2)	0.014(4)	0.008(3)	0.008(2)
$U_{33}$	0.013 (1)	0.014(3)	0.019(3)	0.014(3)
$U_{12}$	0.021(2)	0.015(3)	0.010(3)	0.008(2)
<b>O (2), <math>6h</math>, <math>(x \ y \ 1/4)</math></b>				
$U_{11}$	0.010(1)	0.013(3)	0.008(3)	0.010(2)
$U_{22}$	0.008(1)	0.009(3)	0.004(3)	0.007(2)
$U_{33}$	0.022(1)	0.021(4)	0.026(4)	0.016(3)
$U_{12}$	0.001(1)	0.003(3)	0.003(2)	0.006(2)
<b>O (3), <math>12i</math>, <math>(x \ y \ z)</math></b>				
$U_{11}$	0.023(3)	0.039(4)	0.029(3)	0.025(2)
$U_{22}$	0.014(1)	0.016(3)	0.012(2)	0.013(2)
$U_{33}$	0.010(1)	0.006(2)	0.013(2)	0.006(2)
$U_{12}$	0.012(2)	0.015(3)	0.012(2)	0.011(2)
$U_{13}$	-0.007(2)	-0.008(2)	-0.009(2)	-0.006(2)
$U_{23}$	-0.0035(9)	-0.003(2)	-0.004(2)	-0.003(2)
<b>O (4), <math>2a</math>, <math>(0 \ 0 \ 1/4)</math></b>				
$U_{11}$	0.015(2)	0.014(4)	0.006(3)	0.008(3)
$U_{33}$	0.061(5)	0.034(9)	0.042(9)	0.036(7)

**Table 4.** Calculated BVS of  $\text{Nd}_{(28+x)/3}\text{Al}_x\text{Si}_{6-x}\text{O}_{26}$  crystals at various sites.

Nominal $x$	0	0.5	1.0	1.5
Refined composition	$\text{Nd}_{9.464(8)}\text{Si}_6\text{O}_{26.20(1)}$	$\text{Nd}_{9.77(2)}\text{Al}_{0.5}\text{Si}_{5.5}\text{O}_{26.41(3)}$	$\text{Nd}_{9.78(2)}\text{AlSi}_5\text{O}_{26.17(3)}$	$\text{Nd}_{9.92(2)}\text{Al}_{1.5}\text{Si}_{4.5}\text{O}_{26.13(3)}$
Nd(1), $4f$	2.85(1)	2.91(2)	2.90(2)	2.97(2)
Nd(2), $6h$	2.91(1)	2.88(2)	2.89(2)	2.88(1)
Si, $6h$	4.20(3)	3.96(5)	3.97(4)	3.85(3)
Al, $6h$	-	4.00(4)	4.02(4)	3.89(3)
O(1), $6h$	2.03(2)	2.06(3)	2.06(3)	2.07(2)
O(2), $6h$	2.10(1)	2.10(2)	2.12(2)	2.13(2)
O(3), $12i$	1.93(2)	1.92(2)	1.92(2)	1.91(1)
O(4), $2a$	2.1176(9)	2.024(2)	2.031(2)	2.004(2)

**Table 5.** Comparison of conductivities at various temperatures for as-grown crystals including the high and low temperature activation energies (high temperature in brackets).

	Activation energy (eV)	Conductivity ( $\text{Scm}^{-1}$ )		
		at 300°C	at 500°C	at 800°C
$x = 0$				
c-axis 0.63 (0.40)		$2.7 \times 10^{-3}$	$5.2 \times 10^{-2}$	$2.8 \times 10^{-1}$
⊥ c-axis 0.61 (0.59)		$1.1 \times 10^{-4}$	$1.6 \times 10^{-3}$	$1.3 \times 10^{-2}$
$x = 1.0$				
c-axis 0.81 (0.62)		$4.8 \times 10^{-4}$	$1.6 \times 10^{-2}$	$1.7 \times 10^{-1}$
⊥ c-axis 0.70 (0.66)		$1.8 \times 10^{-4}$	$5.3 \times 10^{-3}$	$5.0 \times 10^{-2}$
$x = 1.5$				
c-axis 0.82 (0.70)		$1.3 \times 10^{-4}$	$6.9 \times 10^{-3}$	$8.9 \times 10^{-2}$
⊥ c-axis 0.79 (0.65)		$7.5 \times 10^{-5}$	$3.5 \times 10^{-3}$	$4.1 \times 10^{-2}$

**Table 6.** Comparison of the  $c$ -axis conductivities for various temperatures as a function of  $x$  doping of Al (high temperature activation energy in brackets).

	Activation energy (eV)	Conductivity ( $\text{Scm}^{-1}$ )		
		at 300°C	at 500°C	at 800°C
$x = 0$ 0.63 (0.40)		$2.7 \times 10^{-3}$	$5.2 \times 10^{-2}$	$2.8 \times 10^{-1}$
$x = 0.5$ 0.73 (0.53)		$1.6 \times 10^{-3}$	$3.7 \times 10^{-2}$	$3.0 \times 10^{-1}$
$x = 1.0$ 0.81 (0.62)		$4.8 \times 10^{-4}$	$1.6 \times 10^{-2}$	$1.7 \times 10^{-1}$
$x = 1.5$ 0.82 (0.70)		$1.3 \times 10^{-4}$	$6.9 \times 10^{-3}$	$8.9 \times 10^{-2}$

**Table 7.** Comparison of the  $ab$  basal plane conductivities for various temperatures as a function of  $x$  doping of Al (high temperature activation energy in brackets).

	Activation energy (eV)	Conductivity ( $\text{Scm}^{-1}$ )		
		at 300°C	at 500°C	at 800°C
$x = 0$ 0.61 (0.59)		$1.1 \times 10^{-4}$	$1.6 \times 10^{-3}$	$1.3 \times 10^{-2}$
$x = 1.0$ 0.70 (0.66)		$1.8 \times 10^{-4}$	$5.3 \times 10^{-3}$	$5.0 \times 10^{-2}$
$x = 1.5$ 0.79 (0.65)		$7.5 \times 10^{-5}$	$3.5 \times 10^{-3}$	$4.1 \times 10^{-2}$

**Table 8.** Comparison of the  $c$ -axis conductivities for the undoped crystal annealed at 850°C for various time.

	Activation energy (eV)	Conductivity ( $\text{Scm}^{-1}$ )		
		at 300°C	at 500°C	at 800°C
As-prepared	0.63 (0.40)	$2.7 \times 10^{-3}$	$5.2 \times 10^{-2}$	$2.8 \times 10^{-1}$
1-month	0.64 (0.59)	$3.4 \times 10^{-4}$	$7.0 \times 10^{-3}$	$5.5 \times 10^{-2}$
2-month	0.67 (0.62)	$9.1 \times 10^{-5}$	$2.3 \times 10^{-3}$	$2.2 \times 10^{-2}$
3-month	0.71 (0.65)	$4.4 \times 10^{-5}$	$1.3 \times 10^{-3}$	$1.3 \times 10^{-2}$

**Table 9.** Comparison of the  $c$ -axis conductivities for the Al-doped crystal (for  $x = 0.5$ ) annealed at 850°C for various time.

	Activation energy (eV)	Conductivity ( $\text{Scm}^{-1}$ )		
		at 300°C	at 500°C	at 800°C
As-prepared	0.73 (0.53)	$1.6 \times 10^{-3}$	$3.7 \times 10^{-2}$	$3.0 \times 10^{-1}$
1-month	0.63 (0.69)	$2.5 \times 10^{-4}$	$4.9 \times 10^{-3}$	$5.4 \times 10^{-2}$
2-month	0.68 (0.66)	$1.3 \times 10^{-4}$	$3.5 \times 10^{-3}$	$4.1 \times 10^{-2}$
3-month	0.73 (0.72)	$1.1 \times 10^{-4}$	$2.9 \times 10^{-3}$	$3.5 \times 10^{-2}$

**Table 10.** Atomic positions and displacement parameters from single crystal X-ray diffraction of  $\text{Nd}_{(28+x)/3}\text{Al}_x\text{Si}_{6-x}\text{O}_{26}$  for  $x = 0$  and  $0.5$  annealed at  $850^\circ\text{C}$  for 3 months.

Nominal x	0	0.5
Refined composition	$\text{Nd}_{9.35(1)}\text{Si}_6\text{O}_{26.002(6)}$	$\text{Nd}_{9.51(1)}\text{Al}_{0.5}\text{Si}_{5.5}\text{O}_{26.012(6)}$
GOF	1.86	2.30
R (%)	2.59	2.33
$R_w$ (%)	7.02	7.07
Nd (1), 4f, (1/3 2/3 z)		
z	-0.00093(6)	-0.00052(7)
Occupancy	0.837(3)	0.877(3)
$U_{11}$	0.0096(2)	0.0092(2)
$U_{33}$	0.0273(3)	0.0161(3)
Nd (2), 6h, (x y 1/4)		
x	0.23102(3)	0.23154(4)
y	-0.01124(3)	-0.01036(4)
$U_{11}$	0.0100(2)	0.0080(2)
$U_{22}$	0.0082(2)	0.0065(2)
$U_{33}$	0.0094(2)	0.0075(2)
$U_{12}$	0.0051(1)	0.0042(1)
Si/Al, 6h, (x y 1/4)		
x	0.4001(2)	0.4007(2)
y	0.3713(2)	0.3716(2)
$U_{11}$	0.0078(6)	0.0053(7)
$U_{22}$	0.0084(6)	0.0060(7)
$U_{33}$	0.0080(5)	0.0065(7)
$U_{12}$	0.0050(5)	0.0035(6)
O (1), 6h, (x y 1/4)		
x	0.3202(6)	0.3195(7)
y	0.4854(6)	0.4861(7)
$U_{11}$	0.034(2)	0.026(3)
$U_{22}$	0.028(2)	0.020(3)
$U_{33}$	0.018(2)	0.017(2)
$U_{12}$	0.026(2)	0.019(2)
O (2), 6h, (x y 1/4)		
x	0.5952(5)	0.5974(6)
y	0.4728(5)	0.4734(6)
$U_{11}$	0.011(2)	0.010(2)
$U_{22}$	0.011(2)	0.010(2)
$U_{33}$	0.023(2)	0.022(3)
$U_{12}$	0.003(1)	0.003(2)
O (3), 12i, (x y z)		
x	0.3435(5)	0.3442(6)
y	0.2521(4)	0.2523(5)
z	0.0662(4)	0.0646(5)
$U_{11}$	0.054(2)	0.041(2)
$U_{22}$	0.016(1)	0.014(2)
$U_{33}$	0.015(1)	0.013(2)
$U_{12}$	0.017(2)	0.014(2)
$U_{13}$	-0.019(2)	-0.013(2)
$U_{23}$	-0.006(1)	-0.004(1)
O (4), 2a, (0 0 1/4)		
$U_{11}$	0.012(2)	0.010(2)
$U_{33}$	0.041(4)	0.032(5)

## REFERENCES

- Carrette, L.; Friedrich, K. A.; Stimming, U., Fuel Cells - Fundamentals and Applications. *Fuel Cells* **2001**, 1, (1), 5-39.
- Ishihara, T.; Sammes, N. M.; Yamamoto, O., Electrolytes. In *High Temperature Solid Oxide Fuel Cells: Fundamentals, Design and Applications*, Singhal, S.; Kendall, K., Eds. Elsevier: Oxford, 2003; pp 83-117.
- Nakayama, S.; Kagayama, T.; Aono, H.; Sadoaka, Y., Ionic conductivity of lanthanoid silicates,  $\text{Ln}_{10}(\text{SiO}_4)_6\text{O}_3$  (Ln = La, Nd, Sm, Gd, Dy, Y, Ho, Er and Yb). *Journal of Materials Chemistry* **1995**, 11, 1801-1806.
- Baikie, T.; Pramana, S. S.; Ferraris, C.; Huang, Y.; Kendrick, E.; Knight, Kevin S.; Ahmad, Z.; White, T. J., Polysomatic apatites. *Acta Crystallographica Section B* **2010**, 66, (1), 1-16.
- Abram, E. J.; Sinclair, D. C.; West, A. R., A novel enhancement of ionic conductivity in the cation-deficient apatite  $\text{La}_{9.33}(\text{SiO}_4)_6\text{O}_2$ . *Journal of Materials Chemistry* **2001**, 11, (8), 1978-1979.
- Arikawa, H.; Nishiguchi, H.; Ishihara, T.; Takita, Y., Oxide ion conductivity in Sr-doped  $\text{La}_{10}\text{Ge}_6\text{O}_{27}$  apatite oxide. *Solid State Ionics* **2000**, 136, 31-37.
- Nakayama, S.; Sakamoto, M., Electrical properties of new type high oxide ionic conductor  $\text{RE}_{10}\text{Si}_6\text{O}_{27}$  (RE = La, Pr, Nd, Sm, Gd, Dy). *Journal of the European Ceramic Society* **1998**, 18, (10), 1413-1418.
- Slater, P. R.; Sansom, J. E. H.; Tolchard, J. R., Development of apatite-type oxide ion conductors. *The Chemical Record* **2004**, 4, (6), 373-384.
- Tolchard, J. R.; Islam, M. S.; Slater, P. R., Defect chemistry and oxygen ion migration in the apatite-type materials  $\text{La}_{9.33}\text{Si}_6\text{O}_{26}$  and  $\text{La}_8\text{Sr}_2\text{Si}_6\text{O}_{26}$ . *Journal of Materials Chemistry* **2003**, 13, (8), 1956-1961.
- Pramana, S. S.; Klooster, W. T.; White, T. J., Framework 'interstitial' oxygen in  $\text{La}_{10}(\text{GeO}_4)_5(\text{GeO}_5)\text{O}_2$  apatite electrolyte. *Acta Crystallogr. B* **2007**, 63, 597-602.
- Pramana, S. S.; Klooster, W. T.; White, T. J., A taxonomy of apatite frameworks for the crystal chemical design of fuel cell electrolytes. *J. Solid State Chem.* **2008**, 181, 1717-1722.
- Orera, A.; Sanjuán, M. L.; Kendrick, E.; Orera, V. M.; Slater, P. R., Raman spectroscopy

studies of apatite-type germanate oxide ion conductors: correlation with interstitial oxide ion location and conduction. *J. Mater. Chem.* **2010**, 20, 2170-2175.

13. Orera, A.; Baikie, T.; Panchmatia, P.; White, T. J.; Hanna, J.; Smith, M. E.; Islam, M. S.; Kendrick, E.; Slater, P. R., Strategies for the Optimisation of Oxide Ion Conductivities of Apatite-Type Germanates. *Fuel Cells* **2011**, 11, (1), 10-16.

14. Orera, A.; Baikie, T.; Kendrick, E.; Shin, J. F.; Pramana, S.; Smith, R.; White, T. J.; Sanjuán, M. L.; Slater, P. R., Apatite germanates doped with tungsten: synthesis, structure, and conductivity. *Dalton Trans.* **2011**, 40, 3903-3908.

15. Nakayama, S.; Aono, H.; Sadaoka, Y., *Chem. Lett.* **1995**, 24, 431-432.

16. Tao, S.; Irvine, J. T. S., Preparation and characterisation of apatite-type lanthanum silicates by a sol-gel process. *Mater. Res. Bull.* **2001**, 36, 1245-1258.

17. Celerier, S.; Laberty-Robert, C.; Ansart, F.; Calmet, C.; Stevens, P., Synthesis by sol-gel route of oxyapatite powder for dense ceramics: Applications as electrolytes for solid oxide fuel cells. *J. Eur. Ceram. Soc.* **2005**, 25, 2665-2668.

18. Ferdov, S.; Sá Ferreira, R. A.; Lin, Z., Hydrothermal synthesis, structural investigations, photoluminescence features, and quantum yield of Eu and Eu-Gd silicates with apatite-type structure. *Chem. Mater.* **2006**, 18, 5958-5964.

19. Fuentes, A. F.; Rodríguez-Reyna, E.; Martínez-González, L. G.; Maczka, M.; Hanuza, J.; Amador, U., Room-temperature synthesis of apatite-type lanthanum silicates by mechanically milling constituent oxides. *Solid State Ionics* **2006**, 177, 1869-1873.

20. Porras-Vázquez, J. M.; Losilla, E. R.; León-Reina, L.; Marrero-López, D.; Aranda, M. A. G., Microstructure and Oxide Ion Conductivity in a Dense  $\text{La}_{9.33}(\text{SiO}_4)_6\text{O}_2$  Oxy-Apatite. *Journal of the American Ceramic Society* **2009**, 92, (5), 1062-1068.

21. Sansom, J. E. H.; Richings, D.; Slater, P. R., A powder neutron diffraction study of the oxide-ion-conducting apatite-type phases,  $\text{La}_{9.33}\text{Si}_6\text{O}_{26}$  and  $\text{La}_8\text{Sr}_2\text{Si}_6\text{O}_{26}$ . *Solid State Ionics* **2001**, 139, 205-210.

22. Slater, P. R.; Sansom, J. E. H., *Solid State Phenomena* **2003**, 90-91, 195-200.

23. Masubuchi, Y.; Higuchi, M.; Katase, H.; Takeda, T.; Kikkawa, S.; Kodaira, K.; Nakayama, S., Oxide ion conduction in  $\text{Nd}_{9.33}(\text{SiO}_4)_6\text{O}_2$  and  $\text{Sr}_2\text{Nd}_8(\text{SiO}_4)_6\text{O}_2$  single crystals grown by floating zone method. *Solid State Ionics* **2004**, 166, (1-2), 213-217.

24. Masubuchi, Y.; Higuchi, M.; Kikkawa, S.; Kodaira, K.; Nakayama, S., Single crystal growth and oxide ion conductivity of oxyapatite type Sr-bearing neodymium silicate. *Solid State Ionics* **2004**, 175, 357-360.

25. McFarlane, J.; Barth, S.; Swaffer, M.; Sansom, J.; Slater, P., Synthesis and conductivities of the apatite-type systems,  $\text{La}_{9.33+x}\text{Si}_{6-y}\text{M}_y\text{O}_{26+z}$  (M=Co, Fe, Mn) and  $\text{La}_8\text{Mn}_2\text{Si}_6\text{O}_{26}$ . *Ionics* **2002**, 8, (1), 149-154.

26. Higuchi, M.; Kodaira, K.; Nakayama, S., Growth of apatite-type neodymium silicate single crystals by the floating-zone method. *Journal of Crystal Growth* **1999**, 207, (4), 298-302.

27. Higuchi, M.; Katase, H.; Kodaira, K.; Nakayama, S., Float zone growth and characterization of  $\text{Pr}_{9.33}(\text{SiO}_4)_6\text{O}_2$  and  $\text{Sm}_{9.33}(\text{SiO}_4)_6\text{O}_2$  single crystals with an apatite structure. *Journal of Crystal Growth* **2000**, 218, (2-4), 282-286.

28. Masubuchi, Y.; Higuchi, M.; Kodaira, K., Reinvestigation of phase relations around the oxyapatite phase in the  $\text{Nd}_2\text{O}_3$ - $\text{SiO}_2$  system. *Journal of Crystal Growth* **2003**, 247, (1-2), 207-212.

29. Higuchi, M.; Kodaira, K.; Nakayama, S., Nonstoichiometry in apatite-type neodymium silicate single crystals. *Journal of Crystal Growth* **2000**, 216, (1-4), 317-321.

30. Felsche, J., Rare earth silicates with the apatite structure. *J. Solid State Chem.* **1972**, 5, 266-275.

31. An, T.; Baikie, T.; Wei, F.; Li, H.; Brink, F.; Wei, J.; Ngoh, S. L.; White, T. J.; Kloc, C., Single crystal growth of apatite-type Al-doped neodymium silicates by the floating zone method. *Journal of Crystal Growth* **2011**, 333, (1), 70-73.

32. Munir, Z. A.; Anselmi-Tamburini, U.; Ohyanagi, M., The effect of electric field and pressure on the synthesis and consolidation of materials: A review of the spark plasma sintering method. *Journal of Materials Science* **2006**, 41, (3), 763-777.

33. Hungria, T.; Galy, J.; Castro, A., Spark Plasma Sintering as a Useful Technique to the Nanostructuration of Piezo-Ferroelectric Materials. *Adv. Eng. Mater.* **2009**, 11, (8), 615-631.
34. Galy, J.; Salles, P.; Rozier, P.; Castro, A., Anionic conductors  $\text{Ln}_{2/3}[\text{Bi}_{12}\text{O}_{14}](\text{MoO}_4)_5$  with  $\text{Ln} = \text{La}, \text{Nd}, \text{Gd}, \text{Ho}, \text{Yb}$ . Synthesis–spark plasma sintering–structure–electric properties. *Solid State Ionics* **2006**, 177, (33–34), 2897-2902.
35. Petricek, V.; Dusek, M.; Palatinus, L. *Jana2006. The crystallographic computing system.*, Institute of Physics, Praha, Czech Republic, 2006.
36. Palatinus, L.; Chapuis, G., SUPERFLIP–a computer program for the solution of crystal structures by charge flipping in arbitrary dimensions. *Journal of Applied Crystallography* **2007**, 40, (4), 786-790.
37. Momma, K.; Izumi, F., VESTA: a three-dimesnional visualization system for electronic and structural analysis. *Journal of Applied Crystallography* **2008**, 41, 653-658.
38. Rietveld, H., M, Line profiles of neutron powder-diffraction peaks for structure refinement. *Acta Crystallogr.* **1967**, 22, (1), 151-152.
39. Okudera, H.; Yoshiasa, A.; Masubuchi, Y.; Higuchi, M.; Kikkawa, S., Determinations of crystallographic space group and atomic arrangements in oxide-ion-conducting  $\text{Nd}_{9,33}(\text{SiO}_4)_6\text{O}_2$ . *Zeitschrift für Kristallographie* **2004**, 219, (1-2004), 27-31.
40. Okudera, H.; Yoshiasa, A.; Masubuchi, Y.; Higuchi, M.; Kikkawa, S., Temperature dependence of structural parameters in oxide-ion-conducting  $\text{Nd}_{9,33}(\text{SiO}_4)_6\text{O}_2$ : single crystal X-ray studies from 295 to 900K. *Journal of Solid State Chemistry* **2004**, 177, 4451-4458.
41. Brown, I. D.; Altermatt, D., Bond-valence parameters obtained from a systematic analysis of the Inorganic Crystal Structure Database. *Acta Crystallographica Section B* **1985**, 41, (4), 244-247.
42. Shannon, R. D., Revised Effective Ionic Radii and Systematic Studies of Interatomic Distances in Halides and Chaleogenides. *Acta Crystallographica Section A* **1976**, 32, 751-767.
43. Wang, Y.; Cao, S.; Shao, M.; Yuan, S.; Kang, B.; Zhang, J.; Wu, A.; Xu, J., Growth rate dependence of the  $\text{NdFeO}_3$  single crystal grown by float-zone technique. *Journal of Crystal Growth* **2011**, 318, (1), 927-931.